Robust hole transport material with interface anchors enhances the efficiency and stability of inverted formamidinium–cesium perovskite solar cells with a certified efficiency of 22.3%

Energy & Environmental Science

Accepted Manuscript

This article can be cited before page numbers have been issued, to do this please use: R. Chen, S. Liu, X. Xu, F. Ren, J. Zhou, X. Tian, Z. Yang, X. Guan, Z. Liu, S. Zhang, Y. Zhang, Y. Wu, L. Han, Y. Qi and W. Chen, *Energy Environ. Sci.*, 2022, DOI: 10.1039/D2EE00433J.

ROYAL SOCIETY OF CHEMISTRY

rsc.li/ees

View Article Online
DOI: 10.1039/D2EE00433J

Robust hole transport material with interface anchors enhances efficiency and stability of inverted formamidinium-cesium perovskite solar cells with a certified efficiency of 22.3%

Rui Chen[1,7], Sanwan Liu[1,7], Xiaojia Xu[3,7], Fumeng Ren[1], Jing Zhou[1], Xueying Tian[1], Zhichun Yang [1], Xinyu Guan[1], Zonghao Liu[1,2*], Shasha Zhang[4], Yiqiang Zhang[4], Yongzhen Wu[2*], Liyuan Han[5], Yabing Qi[6] and Wei Chen[1,2*]

[1]Wuhan National Laboratory for Optoelectronics, Huazhong University of Science and Technology, Luoyu Road 1037, Wuhan, 430074, China.

[2]Optics Valley Laboratory, Hubei 430074, China

[3]Shanghai Key Laboratory of Functional Materials Chemistry, East China University of Science & Technology, Shanghai 200237 (China).

[4]School of Materials Science and Engineering, Henan Institute of Advanced Technology, Zhengzhou University, Zhengzhou 450001, (China).

[5]State Key Laboratory of Metal Matrix Composites, Shanghai Jiao Tong University, Shanghai 200240, China.

[6]Energy Materials and Surface Sciences Unit (EMSSU), Okinawa Institute of Science and Technology Graduate University (OIST), 1919-1 Tancha, Onna-son, Kunigami-gun, Okinawa 904-0495, Japan.

[7]These authors contributed equally to this work.

*Corresponding author

E-mail: liuzonghao@hust.edu.cn (Z.L.); wu.yongzhen@ecust.edu.cn (Y.W.); wnlochenwei@mail.hust.edu.cn (W.C.);

Keywords: Perovskite Solar Cells; Functionalized poly(triarylamine); Buried interfaces; Formamidinium-cesium; High efficiency; Long-term stability

Broader context

A pyridine anchoring groups functionalized poly(triarylamine) (p-PY) as hole transport layer was synthesized to enhance the efficiency and stability of the inverted perovskite solar cells (PSCs). When compared with PTAA, the p-PY showed good surface wettability, energy levels, benign interface defect passivation capability, and thermal/light stability for application in inverted PSCs. At last, the p-PY based MA-free device achieved a champion PCE of 22.8% (certified 22.3%). In particular, the resistance to extremely high temperature (≥120 °C) aging, aiming to resolve the hot-spot effect which is a highly risky factor for the real out-door application of PSCs, has been alleviated by taking advantage of both p-PY HTL and MA-free perovskite in this work.

Abstract

Perovskite solar cells (PSCs) require both high efficiency and reliable long-term stability for commercialization. As important as perovskite layer, charge transport layers and their contact with the adjacent perovskite layer also play a crucial role in the efficiency and stability of PSCs. Herein, we report the use of pyridine anchoring groups functionalized poly(triarylamine) (p-PY) as hole transport layer at buried interfaces between the conductive oxide substrate and formamidinium-cesium perovskite layer to enhance the efficiency and stability of the inverted PSCs. The p-PY based device exhibited a record efficiency of 22.8% (certified efficiency of 22.3%) and maintained

View Article Online
DOI: 10.1039/D2EE00433J

97.5% of the initial efficiency after operation under 1-sun equivalent white-light light-emitting diode array illumination with maximum power point tracking at 45 °C for 1000 h, and 94% and 81% of the initial efficiencies after harsh thermal aging at 85 °C for 500 h and at 120 °C for 200 h, respectively.

Introduction

Perovskite solar cells (PSCs) have attracted much attention due to their low-cost easy fabrication and excellent power conversion efficiency over 25%[1]. To date, the highest-efficiency PSCs are based on the n-i-p architecture, in which the hygroscopic lithium salt doped 2,2′,7,7′-tetrakis[N,N-bis(p-methoxyphenyl) amino]-9,9′-spirobifluorene (spiro-OMeTAD) is commonly used as top hole-transporting layer (HTL)[2, 3]. However, the doped spiro-OMeTAD does not show enough intrinsic stability, which largely limits the device's long-term stability[4]. By contrast, inverted (p-i-n) PSCs using intrinsically stable top electron charge transport layers such as [6,6]-phenyl-C61-butyric acid methyl ester (PCBM) or C60 and stable metal electrodes such as Cr/Au, Bi/Ag or Cu have demonstrated superior stability[5-8], making inverted (p-i-n) PSC a promising architecture for future practical application[9-11]. However, the certified highest efficiencies of p-i-n PSCs are still in the range of 22-23%[11-18], largely lagging behind those of the n-i-p PSCs.

To improve the efficiency of p-i-n PSCs, intense research has been deployed including perovskite growth modulation[11], interface and bulk defects passivation of perovskite[12, 14, 16-18], interface layer engineering[15], etc. However, most devices with efficiencies over 20% are based on methylammonium (MA) cation contained

DOI: 10.1039/D2EE00433J

perovskites[19, 20]. Unfortunately, MA component leads to MA based perovskites with poor thermal stability[21, 22], which largely limits the corresponding device's long-term stability. Alternatively, the deployment of formamidinium-cesium (FACs) perovskite in inverted PSCs has demonstrated superior stability even under harsh 1 sun/85 ˚C light-heat aging conditions[5]. However, the PCEs of FACs perovskites based inverted PSCs are usually less than 22%. It is thus highly desirable to further improve the efficiency of inverted FACs perovskites-based PSCs.

To achieve high-efficiency and stable PSCs, tremendous efforts have been made from the aspect of using top charge transport layers (CTLs), stable perovskites and the passivation of perovskite top surface, etc. This is because the strengthening of the top surface of perovskites can passivate defects and improve perovskite stability[23]; the top CTLs not only enable good charge extraction/transportation but also naturally protect the underneath perovskite from inward penetration of metal electrode and H_2O/O_2, suppress the removal of the volatile species from perovskite[24]. An ideal top CTL should first possess the basic functions of CTLs including suitable energy level, high conductivity and uniform morphology. Besides, it should also possess good intrinsic chemical, thermal, light, and bias stability. In general, preparing CTLs on top of perovskite layer is technically difficult because of the brittle nature of underneath perovskite. Thus, the deposition of top CTLs should avoid detrimental solvent, high temperature (typically <150 ˚C) and high-energy electron or plasma irradiations. As important as these top layers and interfaces, the buried interfaces between the transparent conductive oxide (TCO) substrate and perovskite layer, i.e., TCO/CTL

View Article Online
DOI: 10.1039/D2EE00433J

interface and CTL/perovskite interface, also contribute to the efficiency and stability of PSCs, especially when considering the loose interfacial contact and interfacial delamination between the hard conductive oxide substrate and soft perovskite layer induced by the interfacial built-in stress due to their mismatched coefficient of thermal expansion[25-27]. Such an effect is particularly crucial for the thermal stability and light-heat stability of PSCs during practical application[26]. Moreover, the buried interfaces of PSCs also contain numerous under-coordinated Pb^{2+} defects, which could lead to serious nonradiative recombination causing large open-circuit voltages (V_{OC}) loss[28, 29]. In inverted PSCs, poly[bis(4-phenyl)(2,4,6-trimethylphenyl)amine (PTAA) is the most commonly used organic hole transport material at the buried interface for the devices with efficiencies over 20%[12, 16]. Nevertheless, PTAA does not have a strong chemical interaction with conductive oxide substrate as well as perovskite, and usually sophisticated surface treatments or p-type doping is required to achieve high efficiencies on account of their hydrophobicity[30, 31] and low carrier mobility[32, 33]. This inspires us to upgrade the molecular structure of PTAA to develop a new hole transport material with the function of toughening the buried interfaces between the conductive substrate and perovskite layer as well as passivating defects at the buried interface of the perovskite layer in inverted PSCs.

Here, we introduce pyridine rings as anchoring groups into the molecular structure of PTAA to synthesize a new hole transport material (denoted as p-PY) as HTL for $Cs_{0.15}FA_{0.85}Pb(I_{0.95}Br_{0.05})_3$ perovskite based inverted PSCs. When compared with PTAA, p-PY shows improved surface wettability of the perovskite precursor solution, leading

View Article Online
DOI: 10.1039/D2EE00433J

to the growth of high-quality perovskite films. p-PY also possesses enhanced hole mobility, improved energy level alignment with perovskite, and benign interface defect passivation capability, leading to improved interfacial charge extraction and less interfacial V_{OC} loss. As a result, p-PY based devices exhibit a high V_{OC} value of 1.16 V, which is 60 mV higher than that of the PTAA reference ones (1.10 V) in a typical architecture of indium tin oxide (ITO)/HTL/$Cs_{0.15}FA_{0.85}Pb(I_{0.95}Br_{0.05})_3$/ phenethylammonium iodide (PEAI)/[6,6]-phenyl-C61-butyric acid methyl ester (PCBM)/bathocuproine (BCP)/Ag. Furthermore, the p-PY-based device achieves a champion PCE of 22.8% (certified 22.3%), which outperforms the PTAA-based device with a PCE of 20.8%. To the best of our knowledge, this is one of the highest certified PCEs to date for inverted PSCs based on FACs perovskites. In addition, the p-PY HTL gives rise to superior intrinsic thermal/light stability and stronger interaction at the buried interface through the pyridine anchoring groups to release interfacial stress when compared with PTAA, which leads to the p-PY-based device with markedly improved thermal and operation stability. Particularly, the resistance to extremely high temperature ($\geqslant$120 $^{\circ}$C) aging, aiming to resolve the hot-spot effect which is a highly risky factor for the real out-door application of PSCs, has been alleviated by taking advantage of both p-PY HTL and FACs perovskite in this work.

RESULTS AND DISCUSSION

Material Design and Characterization

To chemically modulate the structure of PTAA, the pyridine unit is considered because it is a widely-used Lewis passivator that can coordinate with Pb^{2+}, thus

View Article Online
DOI: 10.1039/D2EE00433J

substantially improve the binding strength and adhesion of the passivation layer on perovskite surface to passivate defects[34]. In addition, the pyridine unit has been employed as an anchoring group for organic dyes in dye-sensitized solar cells[35] and demonstrated strong anchoring capability on the surface of metal oxide material as well as ITO substrate[36]. Besides, pioneering work has demonstrated the effectiveness of using pyridine functional unit to tune the energy level of HTM for n-i-p PSCs[37].The introduction of pyridine anchoring groups into the PTAA structure is believed to make such a new polymer act as a conductive and glued HTL between the conductive oxide substrate and perovskite layer, which simultaneously toughens the buried interfaces to enhance device durability and suppresses interfacial charge recombination to improve device photovoltaic performance. In addition, the introduction of pyridine functional unit can also modulate the energy level of PTAA.

As shown in Figure 1A, the pyridine anchoring groups functionalized PTAA (denoted as p-PY) at buried interfaces is designed to enhance the efficiency and stability of inverted FACs based PSCs. The synthetic route of p-PY is depicted in scheme S1. To compare the cost of p-PY with the commonly used PTAA, the lab synthesis costs of p-PY and PTAA are estimated according to previous reports (Table S1, Scheme S2 and Table S2-3).[38, 39] It is found p-PY shows lower lab synthesis costs than PTAA. The corresponding ^{1}H, ^{13}C NMR spectra, and mass spectrometry data are shown in Figure S1-3. The molecular weight of p-PY is determined to be 5000-8000, which is lower when compared with the commercial PTAA used in this work with molecular weight of 10000-15000.

View Article Online
DOI: 10.1039/D2EE00433J

The optical properties of PTAA and p-PY are measured by ultraviolet-visible (UV-vis) absorption spectroscopy (Figure S4). Both p-PY/$CHCl_3$ solution and film samples show conspicuous blue-shifted absorption peaks when compared with that of PTAA. This is because the pyridine units generate an inductive electron-withdrawing effect on the aromatic rings of the conjugated backbone[40]. It is also found that p-PY exhibits good solubility in common organic solvents, such as chloroform (CF), dichloromethane (CH_2Cl_2), tetrahydrofuran (THF), etc. However, it shows marginal solubility in highly polar solvents such as N,N-dimethylformamide (DMF) and dimethyl sulfoxide (DMSO), hence ensuring good solution processability and tolerance to perovskite precursor solutions. It should be mentioned that p-PY does not show good solubility in chlorobenzene, thus we use chloroform as the solvent to prepare p-PY solution in following study. For inverted PSCs, the excellent optical transparency of HTL is highly desirable[41]. As shown in Figure S5, the p-PY film on ITO shows slightly higher transparency than that of PTAA at the wavelength range of 350-400 nm and nearly identically good transparency at the wavelength range of 400-900 nm. Their optical bandgaps (Eg^{opt}) are calculated to be 2.94 and 2.98 eV for PTAA and p-PY, respectively, based on the film absorption edges (Table S4).

Electrochemical properties of HTLs were further characterized to determine the HOMO level and the lowest unoccupied molecular orbital (LUMO) level (Figure S6 and Table S4). Ultraviolet photoemission spectroscopy (UPS) measurements were also used to further determine their energy levels in solid state (Figure 1C). The HOMO levels of p-PY and PTAA are calculated to be −5.56 and −5.15 eV, respectively, from

View Article Online
DOI: 10.1039/D2EE00433J

UPS results, which are consistent with those obtained from cyclic voltammetry measurements (Table S4). More importantly, the HOMO level of p-PY matches well the perovskite layer (Figure 1D), which is beneficial for hole extraction[42]. Simultaneously, the LUMO level is high enough to block electron leakage. The p-PY film with thickness around 10 nm measured by step profiler exhibits a smooth and homogeneous surface with a low root-mean-square surface roughness (RMS) of 1.58 nm (Figure S7), benefiting the following multiple layers staking in device fabrication. To evaluate the hole mobilities of two HTLs, space-charge-limited-current (SCLC) measurements were conducted (Figure S8 and Table S4). The p-PY exhibits slightly higher hole mobility (1.93×10^{-4}versus 8.07×10^{-5} cm^2 V^{-1} s^{-1}) and higher conductivity (4.73×10^{-6} versus 2.45×10^{-6} S cm^{-1}) than the PTAA reference (Table S4 and Figure S9), which is likely due to the enhanced inter-chain interactions in the former case.

High intrinsic thermal stability is another essential requirement for HTL. The thermal properties of p-PY and PTAA were examined by thermogravimetric analysis (TGA) and differential scanning calorimetry (DSC) measurements (Figure 1E and Figure S10). It is found that both materials show high decomposition temperature (T_d, corresponding to 5% weight loss point) larger than 400 ˚C, indicating good thermal stability of p-PY and PTAA. However, the glass transition temperatures (T_g) of p-PY and PTAA were measured to be 225 and 108 ˚C, respectively. As a reference, the doped spiro-OMeTAD is reported with a low T_g of ~50 ˚C, which normally leads to the poor thermal stability of the resultant devices[43]. The low T_g of PTAA make it not able to

View Article Online
DOI: 10.1039/D2EE00433J

maintain compact morphology during heating, which is detrimental to device performance. In contrast, the much higher T_g of p-PY than that of PTAA makes the former robust enough to keep stable during the perovskite film's high-temperature annealing process and the long-term thermal stability test of PSCs, especially at the temperature of > 108 °C, at which PTAA cannot sustain its property. The effect of HTLs on device stability will be discussed later. The results above confirm the propriety of p-PY as an effective HTL in inverted PSCs.

Interaction of HTLs and TCO at Buried Interfaces

To investigate the intermolecular interactions between HTLs and ITO substrates, X-ray photoelectron spectroscopy (XPS) measurements were conducted. The samples were prepared by depositing very thin p-PY layer and PTAA layer, respectively, with the corresponding diluted solutions on ITO substrates. As shown in Figure 2A-B, the In *3d* of the ITO in contact with p-PY show a negative energy shift when compared with the PTAA case, indicating the strong interactions between p-PY and perovskite. This result suggests the decrease of cationic charge of In ions in the p-PY/ITO sample, which is likely due to the donation of the lone electron pair on the N atom of the pyridine groups within p-PY to the empty *3d* orbital of In via coordination bonding. The N *1s* also in p-PY sample also shows obvious shift when compared with PTAA. It has been reported that the pyridine is a strong anchoring group in organic light absorbers that have been used in dye sensitized solar cells to enable dye absorption on oxide semiconductors[44, 45], and polymer solar cells to interact with ITO[36]. The pyridine groups in p-PY are considered to interact with ITO through the chemical interaction of pyridine

View Article Online
DOI: 10.1039/D2EE00433J

groups and ITO substrate and thus improve the interface stability.

Interaction of HTLs and Perovskite at Buried Interfaces

The wettability of perovskite precursor solution on the substrate and sequential perovskite growth plays an important role in the perovskite film quality. To study this point, contact angles of DMF (main solvent of perovskite) on two HTL films were measured (Figure S11). p-PY shows a much lower contact angle than that of PTAA (22.4° versus 36.1°) when being contacted by DMF. This suggests p-PY has better wettability when compared with PTAA, which is beneficial to obtain perovskite films with uniform coverage[46]. We further prepared perovskite films on p-PY and PTAA substrates. As shown in Figure S12, the perovskite film deposited on pristine PTAA shows incomplete coverage. Thus, PTAA requires additional DMF pre-washing or poly(9,9-bis(3'-(N,N-dimethyl)-N-ethylammoinium-propyl-2,7-fluorene)-alt-2,7-(9,9-dioctylfluorene))dibromide (PFNBr) treatment to ensure good perovskite quality. When treated PTAA with PFNBr, the deposited perovskite showed full coverage but the obvious rough regions are observed on the sample edge (Figure S12). By contrast, the pristine p-PY film without any treatment can support the growth of a uniform perovskite film on its top with better coverage than the PTAA case even modified with PFNBr. The enhanced wettability is likely due to the introduction of pyridine groups in p-PY that enhance the interaction between the perovskite precursor solution and HTL. In the following study, the PTAA substrates were treated with PFNBr to ensure good perovskite quality. For the p-PY case, the devices with/without PFNBr treatment did not show obvious difference (Figure S13), thus pristine p-PY substrates were used.

View Article Online
DOI: 10.1039/D2EE00433J

Furthermore, scanning electron microscopy (SEM) was used to investigate the effect of HTLs on the morphology of the deposited perovskite films. As shown in Figure S14-15, the perovskite film grown on p-PY exhibits slightly larger grain sizes than the PTAA case (400 nm versus 280 nm). The perovskite film on p-PY also shows a slightly smoother surface with an RMS of 13.9 nm than that of PTAA with an RMS of 14.5 nm (Figure S16). Furthermore, the higher intensity of X-ray diffraction (XRD) peaks of perovskite film on p-PY indicates its improved film crystallinity when compared with that of perovskite film on PTAA (Figure S17). The results confirm that the use of p-PY improves perovskite films quality.

To investigate the intermolecular interactions between HTLs and perovskite, X-ray photoelectron spectroscopy (XPS) measurements were conducted. As shown in Figure 2C, the Pb *4f* peaks of the thin perovskite film in contact with p-PY show a negative energy shift when compared with the PTAA case, indicating the stronger interactions between p-PY and perovskite. This result suggests the decrease of cationic charge of Pb^{2+} ions in the p-PY/perovskite sample, which is likely due to the donation of the lone electron pair on the N atom of the pyridine groups within p-PY to the empty 6p orbital of Pb^{2+} via coordination bonding[47, 48]. It has been reported that the buried interface, i.e., the HTL/perovskite interface in inverted PSCs, also contains numerous under-coordinated Pb^{2+} defects[28]. The p-PY can effectively passivate such defects through its interaction with perovskite. Likewise, the I *3d* signals of the p-PY/perovskite sample exhibit similar negative shifts relative to those of the pristine perovskite film and PTAA/perovskite sample as shown in Figure 2D, suggesting the

View Article Online
DOI: 10.1039/D2EE00433J

strong coordination interactions between the pyridine group within p-PY with Pb^{2+} ions of the perovskite[49].

To better understand the charge-carrier dynamics, we further conducted time-resolved photoluminescence (TRPL) measurements on the HTM/PVK samples with the excitation (Figure S18). The TRPL of perovskite is fast quenched by p-PY and PTAA. The p-PY case shows a lifetime of 7.5 ns which is 37% faster than that of PTAA (Table S5). This further confirms that the hole extraction at HTL/perovskite interface is improved when p-PY is used. This result might be ascribed to the larger energy level offset between the HOMO level of PTAA (−5.15 versus −5.56 eV for p-PY) and the valence band of perovskite (−5.68 eV) (Figure S19).

Photovoltaic Performance

To study the effect of p-PY on device performance, we fabricated inverted PSCs with a configuration of ITO/p-PY/$Cs_{0.15}FA_{0.85}Pb(I_{0.95}Br_{0.05})_3$/PEAI/PCBM/BCP/Ag. About 500 nm thick $Cs_{0.15}FA_{0.85}Pb(I_{0.95}Br_{0.05})_3$ perovskite film was prepared by the one-step antisolvent method[50], PEAI was used to passivate the defects at the top interface[51]. The p-PY thickness was optimized to be ~10 nm by adjusting the solution concentration and rotation speed of spin-coating. It was found that the optimal concentration of p-PY was 0.5 mg mL^{-1} in CF solution (Figure S20). The device's cross-sectional SEM image is shown in Figure S21. The smooth and compact perovskite film with large crystalline grains is clearly observed.

Figure 3A displays the current density-voltage (*J-V*) curves for the optimal devices under the standard AM 1.5G illumination at 100 mW cm^{-2}, and the

View Article Online
DOI: 10.1039/D2EE00433J

corresponding data are summarized in Table S6. Impressively, the p-PY-based devices deliver a champion PCE of 22.8%, with a V_{OC} of 1.16 V, a short-circuit current density (J_{SC}) of 23.80 mA cm^{-2}, and a fill factor (*FF*) of 82.6%, which not only outperforms the control PTAA devices (20.8%), but also is one of the highest values for inverted MA-free PSCs reported to date (Table S7). To verify the reliability of the device performance, we sent one of the non-encapsulated p-PY-based devices to the National Institute of Metrology (NIM, Beijing, China) for certification. The *J-V* curve was measured in air in ambient with a relative humidity of 53%, giving a certified PCE of 22.3%, with a J_{SC} of 23.7 mA cm^{-2}, a V_{OC} of 1.145 V and an *FF* of 82.0% (Figure S22). To further study the output characteristics of the devices and confirm the reliability of the device performance, steady-state photocurrent output measurements at the maximum power point (1.01 V for the p-PY-based device and 0.92 V for the PTAA-based device) were performed. As displayed in Figure 3B, steady-state PCEs of 22.7% and 20.3% were obtained for the p-PY-based and PTAA-based devices, respectively, after 500 s of continuous illumination. To study the effect of HTLs on hysteresis of the devices, we measured the *J-V* curves of the devices based on p-PY and PTAA at both forward scan and reverse scan with scan rate of 5, 50, 150 and 500 mV s^{-1}. It is found that p-PY based device shows less hysteresis with lower hysteresis indexes when compared with the PTAA case (Figure 3C-D and Table S8). This is likely due to the enhanced charge extraction at HTL/perovskite interface and improved charge transportation in HTL, which reduces the charge accumulation at interfaces leading to less hysteresis[52]. In addition, we confirmed the reproducibility of the corresponding

View Article Online
DOI: 10.1039/D2EE00433J

devices as shown in Figure 3E and Figure S23.

Moreover, we measured the external quantum efficiency (EQE) spectra to verify the reliability of the *J-V* curves. As shown in Figure 3F, both devices possess a high photo-response throughout the entire spectrum from 300 to 800 nm, attributed to their similar absorption of the FACs perovskite with a bandgap of 1.54 eV (Figure S24). The integrated J_{SC} values calculated from the full EQE spectrum are 23.58 and 23.52 mA cm^{-2} for the p-PY-based and PTAA-based devices, respectively, which are consistent with the values obtained from the *J-V* measurements.

We also checked the compatibility of p-PY with the commonly used FAMACs perovskite in p-i-n PSCs. As shown in Figure S25, p-i-n PSC based on structure of ITO/p-PY/$Cs_{0.05}(FA_{0.85}MA_{0.15})_{0.95}Pb(I_{0.85}Br_{0.15})_3$/PEAI/PCBM/BCP/Ag gave a PCE of 23.8%, which is also comparable with the reported highest PCEs of p-i-n PSCs (Table S7). This result also suggested that p-PY is a promising HTL for the further improvement of efficiency of p-i-n PSCs with additional optimization strategies in the near future. From the above devices' photovoltaic performance, we could see that the elevated V_{OC} and *FF* of p-PY-based devices are the major causes of the improved PCE. The elevated V_{OC} is related to the better energy level alignment, enhanced charge extraction and suppressed charge recombination in the p-PY-based device. The improved conductivity of p-PY leads to a higher *FF* of p-PY-based devices than the PTAA-based ones. We further analyzed the voltage deficit in the devices, which is defined as the difference between the bandgap/e (e is the elementary charge) and the measured V_{OC}. Based on the bandgap of the MA-free perovskite used in this work (1.54

View Article Online
DOI: 10.1039/D2EE00433J

eV for the absorption threshold), the voltage deficit is calculated to be 0.38 and 0.44 V for p-PY and PTAA based devices, respectively. A low V_{OC} loss is expected to be accompanied by high luminescence yields under open-circuit conditions. Moreover, the determination of V_{OC} is based on the detailed balance principle of photon emission and absorption, and it could be calculated based on the following equations[53]

$$J_{em,0} = q \int_0^{\infty} \mathrm{EQE_{PV}}(\mathrm{E}) \cdot \emptyset_{\mathrm{BB,300K}}(\mathrm{E})\mathrm{dE} \quad (1)$$

$$V_{OC} = \frac{k_B T}{q} \mathrm{In}(\mathrm{EQE_{EL}} \frac{J_{ph}}{J_{em,0}} + 1) \quad (2)$$

Where q is the elementary charge, $\mathrm{EQE_{PV}}(\mathrm{E})$ is the external quantum efficiency, $\emptyset_{\mathrm{BB,300K}}$ is the black body emission spectrum at 300 K, J_{ph} is the photocurrent of the device under light illumination and $J_{\mathrm{em,0}}$ is the current of re-emitted photons at thermal equilibrium. We measured the electroluminescence (EL) of the solar cells operated as light emitting diodes (LEDs) in the dark and under a voltage bias. As shown in Figure 4A, the p-PY-based device shows an obvious EL peak, while an extremely weak EL peak is observed for the device with PTAA. This observation indicates that the charge recombination in the p-PY-based device is much slower than the device with PTAA, which agrees well with the increase in V_{OC} values observed for the p-PY based PSCs. In addition, it is encouraging that the p-PY based device showed EL efficiency close to 5% for a driving current density similar to the short circuit current density (Figure 4B). For comparison, the PTAA-based device only shows EL efficiency of 0.5% under the same injection current. Based on equation (2), it can be estimated that the V_{OC} improvement (ΔV_{OC}) is: $\Delta V_{OC} = k_B T/q\mathrm{In}(\mathrm{EQE_{p\text{-}PY}}/\mathrm{EQE_{PTAA}}) = 0.054$ V, which is consistent with the *J-V* results. Hence, we conclude that the suppressed interface

View Article Online
DOI: 10.1039/D2EE00433J

recombination is an important factor that responsible for the reduced non-radiative recombination in the device based on p-PY. This largely contributes to the improvement of V_{OC}, which is due to the effective passivation of defects at the buried interface and the improved perovskite film quality. Moreover, the improved energy level alignment of p-PY with perovskite could also reduce the V_{OC}-loss due to the reduced free energy loss of charge carrier when compared with PTAA case (Figure S18). To understand the charge carrier dynamics in the devices, light-intensity dependent *J-V* properties were conducted. It is known that the slope of V_{OC} value is greater than k_BT/q if V_{OC} is strongly light intensity dependent, which could be ascribed to the trap-assisted Shockley-Read-Hall (SRH) recombination[5]. By contrast, bimolecular recombination dominates when the slope of V_{OC} is equal to k_BT/q. As shown in Figure 4C, the p-PY-based device shows a much smaller slope of $1.21k_BT/q$ in comparison to that of the optimized PTAA-based device with a slope of $1.56k_BT/q$. This result indicates that the p-PY could effectively retard the monomolecular SRH recombination due to fewer defects in the perovskite film with improved quality, which results in a higher shunt resistance and enhanced device performance. To further investigate the use of p-PY on charge carrier dynamics in the devices, transient photocurrent (TPC) and transient photovoltage (TPV) measurements were conducted. It is found that the charge-recombination lifetime (τ_r) of the p-PY-based device was substantially longer than that of the device based on PTAA (145.4 μs versus 96.5 μs) (Figure 4D), which further verifies the slower charge recombination p-PY based devices, as concluded from the EL measurement. This is due to the improved perovskite quality induced by the use of p-PY and also its defects

passivation capability. This result is also consistent with the higher V_{OC} of the corresponding devices. As shown in Figure S26, the p-PY-based device exhibits a faster charge transfer lifetime (τ_t) than that of PTAA device (4.36 μs versus 7.86 μs), which could be attributed to the improved energy alignment of p-PY with perovskite and the enhanced conductivity of p-PY.

In above, p-PY has showed improved photovoltaic performance when compared with PTAA. The fundamental mechanism of the device performance improvement is mainly assigned to three factors: the effective passivation of defects at buried interface which benefits the improvement of V_{OC} and J_{SC}; the improve energy level alignment and charge transfer between p-PY and perovskite reduce the additional V_{OC}-loss and contribute to the improvement of J_{SC} and *FF*; the improved conductivity of p-PY facilitates the charge transportation and improves the *FF* of the devices.

The employment of p-PY in flexible PSCs were also explored. The p-PY based flexible device gave higher efficiency than the PTAA case (21.1% *versus* 19.6%) (Figure S27 and Table S9), which is consist with the results of devices based on glass/ITO substrate. The flexible devices were also subjected to the bending test and the PCEs evolution were characterized (Figure S28). It was found that the p-PY based device showed better mechanical stability than the PTAA case. This is likely due to the interaction of p-PY with both perovskite and ITO substrate contributes to the interface stability, which is also important to the operational stability. To further verify this point, we tested the stickiness by preparing perovskite films on p-PY and PTAA based flexible substrate by bending experiments. No obvious creases are found on the p-PY based

View Article Online
DOI: 10.1039/D2EE00433J

sample with a bending radius of 5 mm for bending 200 times, but obvious cracks are found on the PTAA based sample (Figure S29). To further check the microscopic morphology of the samples after bending, we tested top-view SEM and the results are shown in Figure S30. Obvious cracks are observed on the PTAA based sample but the p-PY one does not show such obvious cracks. The results indicate that the employ of p-PY could release the interface stress due to its glue-like interaction with both perovskite and ITO substrate and thus improve the mechanical stability of flexible PSCs. This improvement is believed to benefit the operational stability of PSCs.

PSCs' Harsh Thermal and Operational Stability

Besides high efficiency, simultaneously achieving long-term stability is also essential for the commercialization of PSCs. The intrinsic stability of HTLs contributes to the whole device's stability[54]. In order to further explore the intrinsic stability of the two HTLs, we investigated the electrical conductivity change of the thin films against thermal stress by performing conductive atomic force microscopy (c-AFM) measurements. As presented in Figure 5A-B, their c-AFM difference for the fresh films matches well with their conductivity measurement. However, the conductivity of PTAA is greatly reduced relative to p-PY after aging at 120 °C for 200 h in N_2 atmosphere (Figure 5C-D), which is suggested to be associated with crystallization of PTAA during thermal aging due to its lower T_g of 108 °C. Similar phenomena have been reported for spiro-OMeTAD even at the low temperature range of 60-80 °C[43]. Indeed, 120 °C is out of the normal range required by the terrestrial photovoltaic applications, but the well-known hot-spot effect can lead to solar cells reaching such a high temperature[55]. Besides,

the annealing temperature of perovskite film deposited on HTL may reach 150 °C or even higher for all inorganic perovskite, therefore, higher T_g up to 225 °C for p-PY is beneficial for high-efficiency device fabrication and long-term thermal stability of the device.

To further study the influence of p-PY on the devices' thermal stability, we measured the unencapsulated device stability under harsh thermal stress at temperatures of 85 °C and 120 °C in a N_2 atmosphere (Figure 5E). The thermal aging test at 85 °C is in accordance with standard IEC 61215-1:2006 and ISOS-D-2I protocol[56]. A N_2 atmosphere was chosen to exclude the impact of moisture and oxygen on the device's stability caused by imperfect encapsulation. The metal electrode of the devices for stability test is composed of Bi/Ag according to our previous work[7]. This is due to the good intrinsic stability of Bi, which makes Bi a robust interfacial barrier material that can prevent the inward migration of Ag and outward diffusion of corrosive perovskites decomposition by-product, enabling improved device stability[7]. The devices with Bi/Ag electrode showed a similar efficiency to the Ag electrode based devices (Figure S31). For the device performance measurements for different aging time, the devices were cooled down to room temperature and then subjected to *J-V* measurements. Six identically prepared devices were aged at each condition respectively. As a result, the devices based on p-PY and PTAA maintained over 94% and 89% of their initial PCEs after 85 °C thermal aging tests for 500 h in N_2, respectively. It seems that at the temperature below T_g of PTAA, the difference on the two HTLs based devices' thermal stability is not so large. But in contrast, after 120 °C thermal aging tests for 200 h, the

View Article Online
DOI: 10.1039/D2EE00433J

p-PY based device retained over 81% of its initial PCE, the PTAA based device dropped ~50% of its initial PCE (Figure 5E and Figure S32). The stability of the devices shows good reproducibility. These dramatically different behaviors should be mainly due to the low Tg (108 °C) of PTAA make it not able to maintain good morphology and its degradation at 120 °C and also the deteriorated buried interfaces because of the mismatched coefficient of thermal expansion of perovskite, PTAA and ITO. By contrast, the much higher Tg (225 °C) and intrinsic thermal stability of p-PY enable it keep its uniform morphology even at high temperature over 120 °C. Moreover, p-PY with pyridine anchoring groups could act as a glued interface layer to release the interfacial stress to improve device stability[57]. To investigate the thermal stability of PSCs at such a high temperature of >100 °C has rarely been reported before. Although ISOS standard does not involve the high temperature aging at 120 °C, it is of practical importance for the outdoor application of PSCs in view of the hot-spot effect[55]. Even for the commercialized Si-solar cells based on thermally stable light-absorber, the hot-spot effect still constitutes a typical failure mechanism. In order to further improve the stability of PSCs at this extremely high temperature range in the future, we suggest beyond a thermally stable HTL like p-PY as demonstrated in this work, a thermally more stable perovskite film, a more chemically inert electrode and a non-permeable encapsulation technology should be simultaneously integrated into a single device.

During device operation, the bias poling plays a significant role in device stability, which is known related to the potential induced degradation (PID) of solar cells[58]. We further compared PTAA and p-PY based devices' photovoltaic behaviors under light

View Article Online
DOI: 10.1039/D2EE00433J

soaking and high bias poling conditions, in which the ionic migration will be accelerated. The steady-state photocurrent output measurements at high bias poling conditions are performed as displayed in Figure S33. The stepwise transient photocurrents of PSCs have been explored from 0 to 1.8 V with a step voltage (ΔV) of 0.3 V and a duration time of 50 s for each step. It is vital to note that 1.8 V is much higher than the V_{OC} of the solar cells, which is chosen to speed up the ion migration, making it easier to recognize the difference between the two HTLs based devices. At low voltages of 0.3, 0.6, and 0.9 V, the two devices show almost no non-steady photocurrent decays, but at a higher polarization bias of 1.2 V, nonsteady photocurrent decay is observed for PTAA based device, but not for the p-PY case. The non-steady photocurrent may be caused by the ion migration within the perovskite layer and/or the charging-discharge mediated by interface traps at HTL/perovskite interface[59, 60]. When further increases the bias to 1.5 and 1.8 V, nonsteady photocurrent decays are observed for the p-PY based device, but the decay is much slower than that of the PTAA case, indicating that the interfacial stability of withstanding high bias poling is much improved when p-PY is used. Besides, *J-V* curves for these two HTLs based devices before and after different bias poling have also been measured (Figure S34). The *J-V* curves of the two devices have no significant change at the relatively low bias (0.3, 0.6 and 0.9 V). However, when the poling bias increases to >1.2 V, the PTAA based device starts to show evident hysteresis and degradation of performance parameters. By contrast, only after 1.8 V bias poling, slight hysteresis and degradation of the *J-V* curves is found for the p-PY based device. The results prove that the p-PY based devices

View Article Online
DOI: 10.1039/D2EE00433J

possess more stable buried interfaces and can resist high bias poling. This is likely due to strong glued interactions between the pyridine groups in p-PY, perovskite layer and ITO substrate, as well as the good intrinsic electrical stability of p-PY.

In addition, we also tested the operation stability of unencapsulated PSCs under continuous 1 sun equivalent white LED light irradiation in N_2 atmosphere at the cell temperature of ~45 °C by referring to the ISOS-L-1I aging conditions[61]. As shown in Figure 5F, the p-PY-based device maintained over 97.5% of initial PCE after operating for 1000 h with continuous power output at the MPP. In contrast, the PTAA-based device maintained around 81% of the initial efficiency under the same test condition. We tested three devices for the two HTLs respectively based on the condition of the multichannel stability test system. The results of other two devices for each case are shown in the Figure S35. Both cases show similar trend as the one in Figure 5F, which suggests the good reproducibility of device stability and further confirms the better stability of p-PY devices than that of PTAA case. Here, we recognize that the good stability under the above thermal and operational conditions should be partially attributed to stabilized buried interfaces and inherently stable FACs-based perovskite film. Moreover, the results in the comparison studies clearly demonstrate that p-PY indeed contributes to the improved device stability, which is due to its better intrinsic thermal/light stability than PTAA, its stronger interaction at the buried interfaces, and/or the improved perovskite film quality deposited atop p-PY.

Conclusion

In this work, we have developed a new HTL p-PY by the introduction of pyridine-

terminated conjugation into the molecular structure of the commonly used PTAA. The p-PY possesses good surface wettability, energy levels, hole mobility, and thermal/light stability for application in inverted PSCs. Impressively, the device with a p-PY HTL showed a PCE of 22.8% (certified efficiency of 22.3%), which is one of the highest PCEs reported to date for an MA-free perovskite-based inverted PSCs. More importantly, good long-term stability was realized for the p-PY-based device, which retained 97.5% of its initial PCE after 1sun light-soaking for 1000 h and maintained over 94% and 81% of its initial PCE after thermal stress at 85 °C and 120 °C for 500 h and 200 h, respectively. We firmly believe that our pyridine-terminated PTAA via molecular engineering is a promising HTL candidate for improving the performance of MA-free PSCs close to their theoretical efficiency limit and real outdoor applications.

View Article Online
DOI: 10.1039/D2EE00433J

EXPERIMENTAL PROCEDURES

Resource Availability

Lead Contact

Further information and requests for resources and materials should be directed to and will be fulfilled by the lead contact, Wei Chen (wnlochenwei@mail.hust.edu.cn)

Materials Availability

This study did not generate new unique materials

Data and Code Availability

This study did not generate any unique datasets or code

Materials

Formamidinium iodide ($CH(NH_2)_2I$ (FAI)) was synthesized according to previous reports[62]. Lead (II) iodide (99.99% metals basis), Lead (II) bromide (>98%), Cesium bromide (>99%), and Bathocuproine (>99%) were purchased from Tokyo Chemical Industry Co., Ltd. Poly(bis(4-phenyl)(2,4,6-trimethylphenyl)amine) (PTAA) was purchased from Xi'an Polymer Light Technology Corporation. PCBM was purchased from Lumtec Co., Taiwan. All other chemicals were purchased from Sigma-Aldrich and used as received. Silver and bismuth with high purity (99.99%) were purchased from Sino-Platinum Metals CO., Ltd.

Synthesis of p-PY

The intermediate materials **3**, N,N-diphenyl-4-(pyridin-4-yl)aniline were synthesized according to the published procedure[63]. Specifically, in a 50 mL Schlenk tube, compound **1**, 4-(diphenylamino)phenyl boronic acid (318.0 mg, 1.1 mmol), compound

View Article Online
DOI: 10.1039/D2EE00433J

2, 4-Iodopyridine (205.0 mg, 1.0 mmol), $Pd(PPh_3)_4$ (24 mg) and dimethoxyethane (DME) (12 mL) were placed under argon atmosphere. Sodium carbonate (318.0 mg, 3.0 mmol) was dissolved in a minimum volume of water (~0.8 mL), then injected into the DME solution of the reactants. After stirring at room temperature for 1 h, the mixed solution was stirred at 90 °C under argon atmosphere for 16 h. The solvent was removed under reduced pressure and the resultant residue was subjected to column chromatography on SiO_2 (petroleum ether: CH_2Cl_2 = 1: 5). The second major, yellow fraction was collected, gave the required product **3** as a yellowish solid (158.4 mg, yield 49.2%). ^{1}H NMR (400 MHz, $CDCl_3$, δ, ppm): 8.60 (d, J=6.04 Hz, 2H), 7.52 (d, J=8.72 Hz, 2H), 7.46-7.48 (m, 2H), 7.27-7.31 (m, 4H), 7.13-7.16 (m, 6H), 7.06-7.10 (m, 2H). Mass spectrometry (ESI-MS, m/z): $[M + Na]^+$ Calc. for $C_{23}H_{19}N_2Na$: 323.1548; found: 323.1553.

The intermediate materials **4**, 4-bromo-N-(4-bromophenyl)-N-(4-(pyridin-4-yl)phenyl)aniline was synthesized according to the published procedure[64]. Compound **3** (500.0 mg, 1.55 mmol), NBS, N-Bromosuccinimide (608.1 mg, 3.42 mmol), 3 drops AcOH and 16 mL chloroform were added to a 250 mL eggplant bottle. After that, the mixed solution was stirred at room temperature for 1h under an argon atmosphere. After 18 h continuously stirring at 50 °C, 10 mL water was added, the mixture was extracted with dichloromethane. The organic phases were combined together, dried over anhydrous Na_2SO_4 and purified by column chromatography on silica gel (petroleum ether: ethyl acetate = 5 : 1) to afford a yellow solid. After DCM/n-hexane recrystallization, the yellow product **4** (603.1 mg, yield 81.4%) was obtained. ^{1}H NMR

View Article Online
DOI: 10.1039/D2EE00433J

(400 MHz, $CDCl_3$, δ, ppm): 8.62 (d, J = 5.56 Hz, 2H), 7.51-7.55 (m, 2H), 7.47 (m, J = 5.56 Hz, 2H), 7.37-7.41 (m, 4H), 7.12-7.14 (m, 2H), 6.98-7.01 (m, 2H). Mass spectrometry (ESI-MS, m/z): $[M + H]^+$ Calc. for $C_{23}H_{17}N_2Br_2$: 478.9758; found: 478.9760.

In a dry 250 mL three-neck round-bottom flask, **4** (724 mg, 1.52 mmol), boracyl alcohol ester (2310 mg, 9.09 mmol), potassium acetate (859 mg, 8.76 mmol), $Pd(dppf)Cl_2$ (200 mg, 0.28 mmol), ultra-dry 1,4-dioxane (36.4 mL) were added and stirred overnight under 90 °C. The reaction quenched by water and the solvent removed under reduced pressure. Column chromatography was then performed (petroleum ether: ethyl acetate = 5: 1) to obtain a pale yellow solid. The solids were recrystallized with n-hexane to give a white solid **5** (0.554 g, yield 63.6%). ^1H NMR (400 MHz, $CDCl_3$, δ, ppm): 8.61-8.63 (m, 2H), 7.71 (d, J = 8.4 Hz, 4H), 7.53 (d, J = 8.64 Hz, 2H), 7.49-7.50 (m,2H), 7.18 (d, J = 8.64 Hz, 2H), 7.11 (d, J = 8.4 Hz, 4H), 1.35 (s, 24H). Mass spectrometry (ESI-MS, m/z): $[M + H]^+$ Calc.for $C_{35}H_{41}B_2N_2O_2$: 575.3252; found: 575.3248.

5 (536.7 mg, 0.93 mmol), **4** (448.7 mg, 0.93 mmol), $Pd(PPh_3)_4$ (20 mg) and degassed toluene (9 mL) were added to a 50 mL Schlenk tube in the glove box. Potassium carbonate (552.0 mg, 4 mmol) was dissolved in 2 mL water and injected into the mixture. The reaction was finished after being stirred at 85 °C for 40 h under an argon atmosphere. After cooling to room temperature, the reaction mixture was dropped into 200 mL methanol. The precipitate was collected by filtration and further purified by Soxhlet extraction with methanol, acetone, then dissolved by Soxhlet extraction with chloroform to afford a yellow solid **p-PY** (386.6 mg).

View Article Online
DOI: 10.1039/D2EE00433J

Device Fabrication

Glass/ITO substrates (15 Ω sq^{-1}) were cleaned through sequential ultrasonication for 20 min in a detergent solution, distilled water, alcohol, and isopropanol. Then, the substrates were dried with N_2 and cleaned by UV ozone for 15 min and finally transferred into a N_2-filled glovebox before use. The PTAA solution was prepared with a concentration of 5 mg mL^{-1} in CB. The as-prepared PTAA solution was spin-coated onto the ITO substrates at 6000 rpm for 30 s and the substrates were subsequently annealed at 100 ˚C for 10 min. In order to increase its surface wetting, a 0.5 mg mL^{-1} PFNBr in methyl alcohol was spin-coated onto the PTAA at 6000 rpm for 30 s. The p-PY solution was prepared with a concentration of 0.25-1.00 mg mL^{-1} in $CHCl_3$. For the p-PY-based devices, the p-PY solution was spin-coated onto the ITO substrates at 1500 rpm for 30 s, and the substrates were subsequently annealed at 100 ˚C for 10 min. The perovskite precursor solution was prepared by dissolving 219.3 mg FAI, 619.5 mg PbI_2, and 0.05 mg CsBr stoichiometrically in a 1 mL mixed solvent of DMF and DMSO with a volume ratio of 4:1. The perovskite solutions were spin-coated onto glass/ITO/HTL at 6000 rpm for 60 s. 150 μL CB was dripped onto the center of the film at 15 s before the end of spin-coating. The as-prepared perovskite films were subsequently annealed on a hotplate at 150 ˚C for 20 min. Then 100 μL of PEAI (1 mg mL^{-1} in IPA) was spin-coated onto the as-prepared perovskite films at the speed of 5000 rpm for 30 s. The film then was heated at 100 ˚C for 10 min. Noted that the PEAI solution needed to be drop on the perovskite film quickly. Then a chlorobenzene solution of PCBM (20 mg ml^{-1}) was spin-coated on top of the PEAI at the rotation speed of 3000 rpm for 30 seconds

View Article Online
DOI: 10.1039/D2EE00433J

and heated at 70 °C for 10 min. In the final step, the BCP (8 nm), and Ag (80 nm) were deposited at high vacuum (less than 5×10^{-4} Pa) while finely controlling the evaporation rate at 0.1, 0.1 and 0.1-0.5 Å s^{-1}, respectively. The Bi/Ag (20 nm/80 nm) electrodes in the devices for stability test were thermally evaporated with a controlled evaporation rate of 0.1 and 0.1 to 0.5 Å s^{-1}, respectively.

Characterization

^{1}HNMR, the nuclear magnetic resonance (NMR) spectra were obtained from a BRUKER AVANCE III 600 MHz NMR Instrument (in $CDCl_3$). MALDI-TOF HRMS was performed on a Bruker Autoflex instrument, using 1,8,9-trihydroxyanthracene as a matrix. Cyclic voltammetry measurements were carried out under argon atmosphere using the CHI760E voltammetric workstation with a N_2-saturated solution of 0.1 M tetra-n-butyl ammonium hexafluoro phosphate (Bu_4NPF_6) in CH_2Cl_2 as the supporting electrolyte. A platinum disk working electrode, a platinum wire counter electrode, and a silver wire reference electrode were employed, and the ferrocene/ferrocenium redox couple (Fc/Fc^+) was used as the reference for all measurements with a scanning rate of 50 mV s^{-1}. TGA analysis was performed using TGA8000 (PerkinElmer Co., USA) under a dry air condition with a heating rate of 10 °C min^{-1}. Differential scanning calorimetry (DSC) was recorded on a PerkinElmer 13 Diamond DSC instrument under nitrogen. Atomic Force Microscopy (AFM) measurements were conducted using a Dimension Icon Scanning Probe Microscope (Asylum Research, MFP-3D-Stand Alone) in the tapping mode. SEM images were obtained using a Nova NanoSEM 450 scanning electron microscope (FEI Co., Netherlands). An XPS system (Thermo ESCALAB

View Article Online
DOI: 10.1039/D2EE00433J

250XI) was used to acquire the XPS spectra. UPS spectra were acquired using a Thermo ESCALAB 250XI instrument equipped with a ^{1}He ultraviolet radiation source (21.22 eV). The crystal structure of the films was characterized using XRD with an Empyrean X-ray diffractometer with Cu Kα radiation (PANalytical B.V. Co., Netherlands). The UV-vis spectra of perovskite films were characterized from a Lambda 950 UV-vis spectrophotometer (PerkinElmer Co., USA). The Steady-state PL spectra were recorded using an Edinburgh FLS920 fluorescence spectrometer (Edinburgh Co., UK) with an excitation source wavelength of 532 nm. The TRPL measurements were conducted by a fluorescence spectrometer with an excitation wavelength of 478 nm (DeltaFlex, Horiba), and the TRPL results are fitted by a bi-exponential rate law model according to the following function: $y = A_1 \exp(-t/\tau_1) + A_2 \exp(-t/\tau_2) + y_0$, where τ_1 and τ_2 are the lifetimes for the fast and slow decays, respectively. Photovoltaic measurements employed a black mask with an aperture area of 0.0902 cm^2 under standard AM1.5G simulated sunlight (Oriel, model 9119) and the simulated light intensity was calibrated with a silicon photodiode (Enlitech). The EQE spectra were obtained by EQE system (Saifan, China) using monochromatic light of 1×10^{16} photons cm^{-2} under DC mode. The EQE-EL spectra were recorded by a LED photoluminescence quantum-yield measurement system (Shenzhen Puyan Internet Technology Co., Ltd) equipped with Keithley 2400 Source Measure Unit. The Mott-Schottky plots, TPV and TPC plots, and space charge limited current (SCLC) plots were obtained by a Zennium electrochemistry workstation (Zahner, Germany). The thermal stability of the unencapsulated PSCs was performed by aging the devices on a hot plate at a

View Article Online
DOI: 10.1039/D2EE00433J

temperature of 120 °C in a N_2 atmosphere. The efficiency of the aged device was measured under a standard solar simulator in air periodically. The operational stability of the unencapsulated PSCs was performed at the MPP tracking under continuous white-light LED array illumination in N_2 atmosphere, the light intensity was calibrated to achieve the same J_{SC} from the PSCs measured under a standard solar simulator (AM 1.5G, 100 mW cm^{-2}), and the cell temperature was controlled at around 45 °C.

ACKNOWLEDGMENTS

This work was financially supported by the National Key Research and Development Project funding from the Ministry of Science and Technology of China (Grant No. 2021YFB3800104), the National Natural Science Foundation of China (51822203, 52002140, U20A20252, 51861145404, 62105293), Young Elite Scientists Sponsorship Program by CAST, the Self-determined and Innovative Research Funds of HUST (2020kfyXJJS008), the Natural Science Foundation of Hubei Province (ZRMS2020001132), Shenzhen Science and Technology Innovation Committee (JCYJ20180507182257563), the Outstanding Young Talents Innovation Team Support Plan of Zhengzhou University and the Innovation Project of Optics Valley Laboratory (Grant No. OVL2021BG008). Y.B.Q. acknowledges the support from the Energy Materials and Surface Sciences Unit of the Okinawa Institute of Science and Technology Graduate University.

AUTHOR CONTRIBUTION

R.C., S.L., X.X. contributed equally to this work. R.C., S. L., X.X, Z.L and W.C. conceived the project and designed the experiments. R.C., S. L., X.X. performed and

View Article Online
DOI: 10.1039/D2EE00433J

were involved in all the experimental parts. R.C., S.L., X.X, S.Z, Y.Z, L.H, Z. L, Y.W, Y. Q. and W.C. co-wrote the paper. F.R, J.Z., X.T, W.C, and X.G contributed materials and analysis tools. Z.L, Y.W and W.C. directed and supervised this project. All authors discussed the results and commented on the manuscript.

DECLARATION OF INTERESTS

The authors declare no competing interests.

View Article Online
DOI: 10.1039/D2EE00433J

References

1. NREL, Best Research-cell Efficiency Chart, https://www.nrel.gov/pv/cell-efficiency.html.

2. J. Jeong, M. Kim, J. Seo, H. Lu, P. Ahlawat, A. Mishra, Y. Yang, M. A. Hope, F. T. Eickemeyer and M. Kim, *Nature*, 2021, **592**, 381-385.

3. J. J. Yoo, G. Seo, M. R. Chua, T. G. Park, Y. Lu, F. Rotermund, Y.-K. Kim, C. S. Moon, N. J. Jeon and J.-P. Correa-Baena, *Nature*, 2021, **590**, 587-593.

4. Z. Hawash, L. K. Ono and Y. Qi, *Adv. Mater. Interfaces*, 2018, **5**, 1700623.

5. Y.-H. Lin, N. Sakai, P. Da, J. Wu, H. C. Sansom, A. J. Ramadan, S. Mahesh, J. Liu, R. D. Oliver and J. Lim, *Science*, 2020, **369**, 96-102.

6. S. Bai, P. Da, C. Li, Z. Wang, Z. Yuan, F. Fu, M. Kawecki, X. Liu, N. Sakai, J. T.-W. Wang, S. Huettner, S. Buecheler, M. Fahlman, F. Gao and H. J. Snaith, *Nature*, 2019, **571**, 245-250.

7. 7. S. Wu, R. Chen, S. Zhang, B. H. Babu, Y. Yue, H. Zhu, Z. Yang, C. Chen, W. Chen, Y. Huang, S. Fang, T. Liu, L. Han and W. Chen, *Nat. Commun.*, 2019, **10**, 1161.

8. Y. Deng, Z. Ni, A. F. Palmstrom, J. Zhao, S. Xu, C. H. Van Brackle, X. Xiao, K. Zhu and J. Huang, *Joule*, 2020, **4**, 1949-1960.

9. Y. Deng, S. Xu, S. Chen, X. Xiao, J. Zhao and J. Huang, *Nat. Energy*, 2021, **6**, 633-641.

10. Z. Yang, W. Zhang, S. Wu, H. Zhu, Z. Liu, Z. Liu, Z. Jiang, R. Chen, J. Zhou, Q. Lu, Z. Xiao, L. Shi, H. Chen, L. K. Ono, S. Zhang, Y. Zhang, Y. Qi, L. Han and W. Chen, *Sci. Adv.*, 2021, **7**, eabg3749.

11. S. Chen, X. Dai, S. Xu, H. Jiao, L. Zhao and J. Huang, *Science*, 2021, **373**, 902-907.

12. F. Li, X. Deng, F. Qi, Z. Li, D. Liu, D. Shen, M. Qin, S. Wu, F. Lin and S.-H. Jang, *J. Am. Chem. Soc.*, 2020, **142**, 20134-20142.

View Article Online
DOI: 10.1039/D2EE00433J

13. F. Li, X. Deng, F. Qi, Z. Li, D. Liu, D. Shen, M. Qin, S. Wu, F. Lin, S.-H. Jang, J. Zhang, X. Lu, D. Lei, C.-S. Lee, Z. Zhu and A. K. Y. Jen, *J. Am. Chem. Soc.*, 2020, **142**, 20134-20142.

14. F. Zhang, S. Ye, H. Zhang, F. Zhou, Y. Hao, H. Cai, J. Song and J. Qu, *Nano Energy*, 2021, 106370.

15. X. Li, Y. Meng, R. Liu, Z. Yang, Y. Zeng, Y. Yi, W. E. Sha, Y. Long and J. Yang, *Adv. Energy Mater.*, 2021, **11**, 2102844.

16. X. Zheng, Y. Hou, C. Bao, J. Yin, F. Yuan, Z. Huang, K. Song, J. Liu, J. Troughton and N. Gasparini, *Nat. Energy*, 2020, **5**, 131-140.

17. M. Degani, Q. An, M. Albaladejo-Siguan, Y. J. Hofstetter, C. Cho, F. Paulus, G. Grancini and Y. Vaynzof, *Sci. Adv.*, 2021, **7**, eabj7930.

18. T. Zhu, L. Shen, S. Xun, J. S. Sarmiento, Y. Yang, L. Zheng, H. Li, H. Wang, J. L. Bredas and X. Gong, *Adv. Mater.*, 2109348.

19. X. Lin, D. Cui, X. Luo, C. Zhang, Q. Han, Y. Wang and L. Han, *Energy Environ. Sci.*, 2020, **13**, 3823-3847.

20. B. Liu, H. Bi, D. He, L. Bai, W. Wang, H. Yuan, Q. Song, P. Su, Z. Zang and T. Zhou, *ACS Energy Lett.*, 2021, **6**, 2526-2538.

21. B. w. Park and S. I. Seok, *Adv. Mater.*, 2019, **31**, 1805337.

22. B. Conings, J. Drijkoningen, N. Gauquelin, A. Babayigit, J. D'Haen, L. D'Olieslaeger, A. Ethirajan, J. Verbeeck, J. Manca, E. Mosconi, F. D. Angelis and H.-G. Boyen, *Adv. Energy Mater.*, 2015, **5**, 1500477.

23. S. He, L. Qiu, L. K. Ono and Y. Qi, *Mater. Sci. Eng. R Rep.*, 2020, **140**, 100545.

24. S. Zhang, Z. Liu, W. Zhang, Z. Jiang, W. Chen, R. Chen, Y. Huang, Z. Yang, Y. Zhang and L.

View Article Online
DOI: 10.1039/D2EE00433J

Han, *Adv. Energy Mater.*, 2020, **10**, 2001610.

25. Z. Dai, S. K. Yadavalli, M. Chen, A. Abbaspourtamijani, Y. Qi and N. P. Padture, *Science*, 2021, **372**, 618-622.

26. W. Yang, D. Zhong, M. Shi, S. Qu and H. Chen, *iScience*, 2019, **22**, 534-543.

27. Q. Dong, C. Zhu, M. Chen, C. Jiang, J. Guo, Y. Feng, Z. Dai, S. K. Yadavalli, M. Hu and X. Cao, *Nat. Commun.*, 2021, **12**, 1-9.

28. X. Yang, D. Luo, Y. Xiang, L. Zhao, M. Anaya, Y. Shen, J. Wu, W. Yang, Y. H. Chiang and Y. Tu, *Adv. Mater.*, 2021, **33**, 2006435.

29. C.-L. Chen, S.-S. Zhang, T.-L. Liu, S.-H. Wu, Z.-C. Yang, W.-T. Chen, R. Chen and W. Chen, *Rare Met.*, 2020, **39**, 131-138.

30. W.-Q. Wu, Q. Wang, Y. Fang, Y. Shao, S. Tang, Y. Deng, H. Lu, Y. Liu, T. Li and Z. Yang, *Nat. Commun.*, 2018, **9**, 1-8.

31. S. Li, Y.-L. Cao, W.-H. Li and Z.-S. Bo, *Rare Met.*, 2021, 1-18.

32. K. Rakstys, C. Igci and M. K. Nazeeruddin, *Chem. Sci.*, 2019, **10**, 6748-6769.

33. H. D. Pham, L. Xianqiang, W. Li, S. Manzhos, A. K. K. Kyaw and P. Sonar, *Energy Environ. Sci.*, 2019, **12**, 1177-1209.

34. H. Zhang, Y. Wu, C. Shen, E. Li, C. Yan, W. Zhang, H. Tian, L. Han and W. H. Zhu, *Adv. Energy Mater.*, 2019, **9**, 1803573.

35. J. Cui, J. Lu, X. Xu, K. Cao, Z. Wang, G. Alemu, H. Yuang, Y. Shen, J. Xu, Y. Cheng and M. Wang, *J. Phys. Chem. C*, 2014, **118**, 16433-16440.

36. G. Chen, S. Liu, Z. He, H.-B. Wu, W. Yang, B. Zhang and Y. Cao, *Polym. Chem.*, 2017, **8**, 6720-6732.

37. B. Xu, Z. Zhu, J. Zhang, H. Liu, C. C. Chueh, X. Li and A. K. Y. Jen, *Adv. Energy Mater.*, 2017, **7**, 1700683.

38. T. P. Osedach, T. L. Andrew and V. Bulović, *Energy Environ. Sci.*, 2013, **6**, 711-718.

39. M. Petrus, T. Bein, T. Dingemans and P. Docampo, *J. Mater. Chem. A*, 2015, **3**, 12159-12162.

40. M. Jeong, I. W. Choi, E. M. Go, Y. Cho, M. Kim, B. Lee, S. Jeong, Y. Jo, H. W. Choi and J. Lee, *Science*, 2020, **369**, 1615-1620.

41. L. Calió, S. Kazim, M. Grätzel and S. Ahmad, *Angew. Chem. Int. Ed.*, 2016, **55**, 14522-14545.

42. Q. Yao, Q. Xue, Z. Li, K. Zhang, T. Zhang, N. Li, S. Yang, C. J. Brabec, H. L. Yip and Y. Cao, *Adv. Mater.*, 2020, **32**, 2000571.

43. N. J. Jeon, H. Na, E. H. Jung, T.-Y. Yang, Y. G. Lee, G. Kim, H.-W. Shin, S. I. Seok, J. Lee and J. Seo, *Nat. Energy*, 2018, **3**, 682-689.

44. J. Cui, J. Lu, X. Xu, K. Cao, Z. Wang, G. Alemu, H. Yuang, Y. Shen, J. Xu and Y. Cheng, *The J. Phys. Chem. C*, 2014, **118**, 16433-16440.

45. M. P. Bolisetty, C.-T. Li, K. J. Thomas, G. B. Bodedla and K.-C. Ho, *Tetrahedron*, 2015, **71**, 4203-4212.

46. C. Bi, Q. Wang, Y. Shao, Y. Yuan, Z. Xiao and J. Huang, *Nat. Commun.*, 2015, **6**, 1-7.

47. N. Ahn, D.-Y. Son, I.-H. Jang, S. M. Kang, M. Choi and N.-G. Park, *J. Am. Chem. Soc.*, 2015, **137**, 8696-8699.

48. L. Zuo, H. Guo, D. W. deQuilettes, S. Jariwala, N. De Marco, S. Dong, R. DeBlock, D. S. Ginger, B. Dunn and M. Wang, *Sci. Adv.*, 2017, **3**, e1700106.

49. Z. Huang, X. Hu, C. Liu, L. Tan and Y. Chen, *Adv. Funct. Mater.*, 2017, **27**, 1703061.

50. X. Sun, Z. Li, X. Yu, X. Wu, C. Zhong, D. Liu, D. Lei, A. K. Y. Jen, Z. a. Li and Z. Zhu, *Angew.*

View Article Online
DOI: 10.1039/D2EE00433J

Chem. Int. Ed., 2021, **133**, 7303-7309.

51. Q. Jiang, Y. Zhao, X. Zhang, X. Yang, Y. Chen, Z. Chu, Q. Ye, X. Li, Z. Yin and J. You, *Nat. Photonics*, 2019, **13**, 460-466.

52. Z. Liu, Q. Chen, J. W. Lee, Z. Zhao, X. Xu, Y. T. Hsieh, L. Meng, P. Sun, N. D. Marco and H. Zhou, *Adv. Energy Mater.*, 2018, **8**, 1800568.

53. W. Shockley and H. J. Queisser, *J. Appl. Phys.*, 1961, **32**, 510-519.

54. Z. Liu, L. Qiu, L. K. Ono, S. He, Z. Hu, M. Jiang, G. Tong, Z. Wu, Y. Jiang and D.-Y. Son, *Nat. Energy*, 2020, **5**, 596-604.

55. P. Holzhey and M. Saliba, *J. Mater. Chem. A*, 2018, **6**, 21794-21808.

56. IEC 61215-1:2016. Terrestrial Photovoltaic (PV) Modules Design Qualification and Type Approval-Part 1: Test Requirements (IEC, 2016).

57. H. Wang, C. Zhu, L. Liu, S. Ma, P. Liu, J. Wu, C. Shi, Q. Du, Y. Hao, S. Xiang, H. Chen, P. Chen, Y. Bai, H. Zhou, Y. Li and Q. Chen, *Adv. Mater.*, 2019, **31**, 1904408.

58. N. Arora, M. I. Dar, A. Hinderhofer, N. Pellet, F. Schreiber, S. M. Zakeeruddin and M. Grätzel, *Science*, 2017, **358**, 768-771.

59. B. Chen, M. Yang, X. Zheng, C. Wu, W. Li, Y. Yan, J. Bisquert, G. Garcia-Belmonte, K. Zhu and S. Priya, *J. Phys. Chem. Lett.*, 2015, **6**, 4693-4700.

60. B. Wu, K. Fu, N. Yantara, G. Xing, S. Sun, T. C. Sum and N. Mathews, *Adv. Energy Mater.*, 2015, **5**, 1500829.

61. M. V. Khenkin, E. A. Katz, A. Abate, G. Bardizza, J. J. Berry, C. Brabec, F. Brunetti, V. Bulović, Q. Burlingame and A. Di Carlo, *Nat. Energy*, 2020, **5**, 35-49.

62. G. E. Eperon, S. D. Stranks, C. Menelaou, M. B. Johnston, L. M. Herz and H. J. Snaith, *Energy*

View Article Online
DOI: 10.1039/D2EE00433J

Environ. Sci., 2014, **7**, 982-988.

63. K. Kowalski, N. Long, M. Kuimova, A. Kornyshev, A. Taylor and A. White, *New J. Chem.*, 2009, **33**, 598-606.

64. J. Zhao, F. Dang, B. Liu, Y. Wu, X. Yang, G. Zhou, Z. Wu and W.-Y. Wong, *Dalton Trans.*, 2017, **46**, 6098-6110.

View Article Online
DOI: 10.1039/D2EE00433J

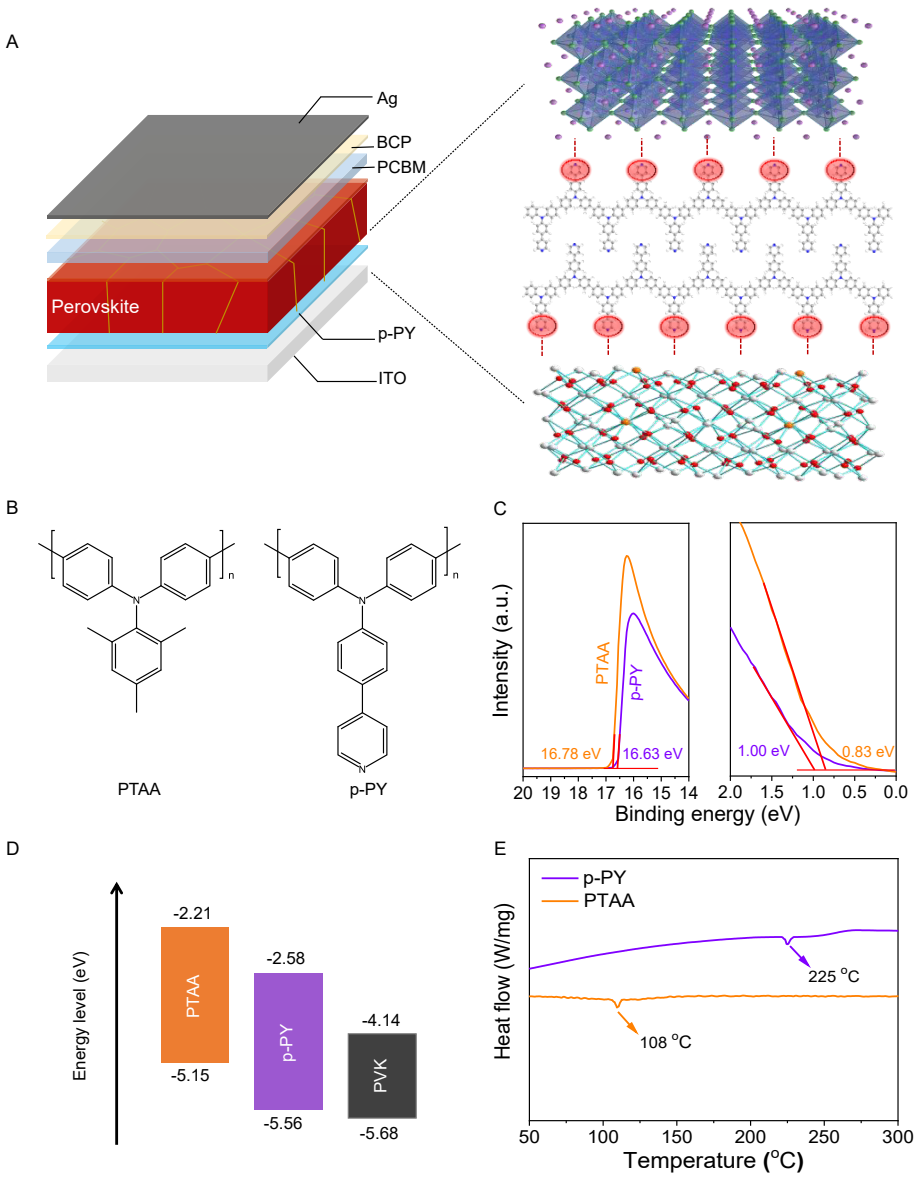

Figure 1. Electronic and thermal properties of the two HTLs studied in this work. (**A**) The schematic illustration of the device structure based on p-PY. (**B**) The molecular structure of p-PY and PTAA. (**C**) The UPS spectra of the ITO/p-PY and ITO/PTAA samples. (**D**) Energy level diagram. (**E**) DSC curves of p-PY and PTAA during the second heating scan, which was measured at a heat ramp of 10 $^{\circ}$C min^{-1}.

View Article Online
DOI: 10.1039/D2EE00433J

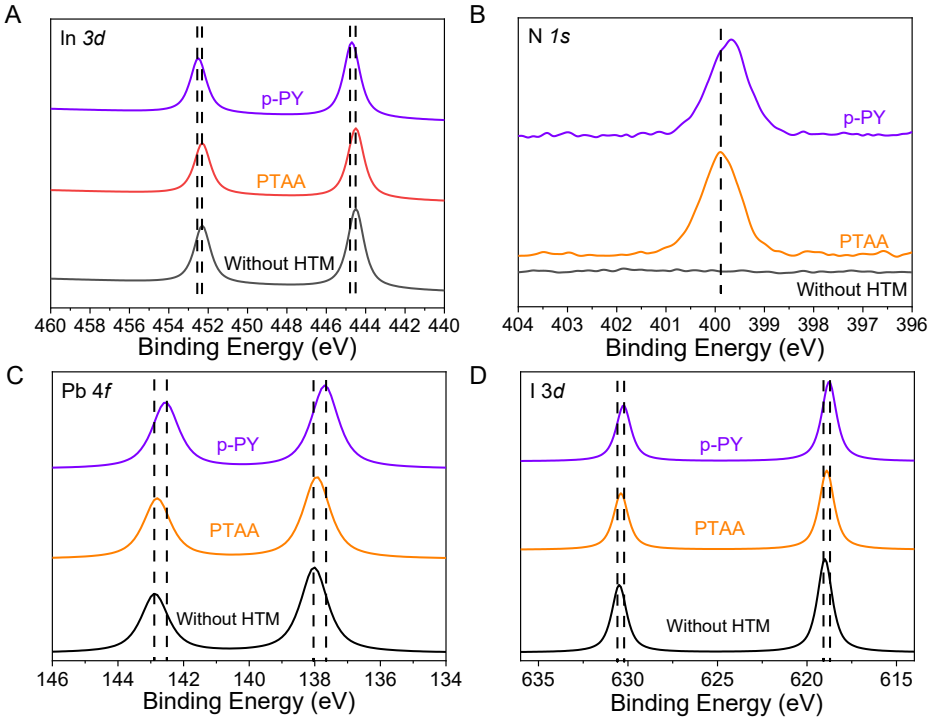

Figure 2. Interaction of HTLs and the perovskite films. High resolution In *3d* (**A**) and N *1s* (**B**) core-level XPS spectra for the ITO and HTLs atop ITO substrates. High resolution Pb *4f* (**C**) and I *3d* (**D**) core-level XPS spectra for the pristine perovskite film and perovskite films atop HTLs deposited on ITO substrates.

View Article Online
DOI: 10.1039/D2EE00433J

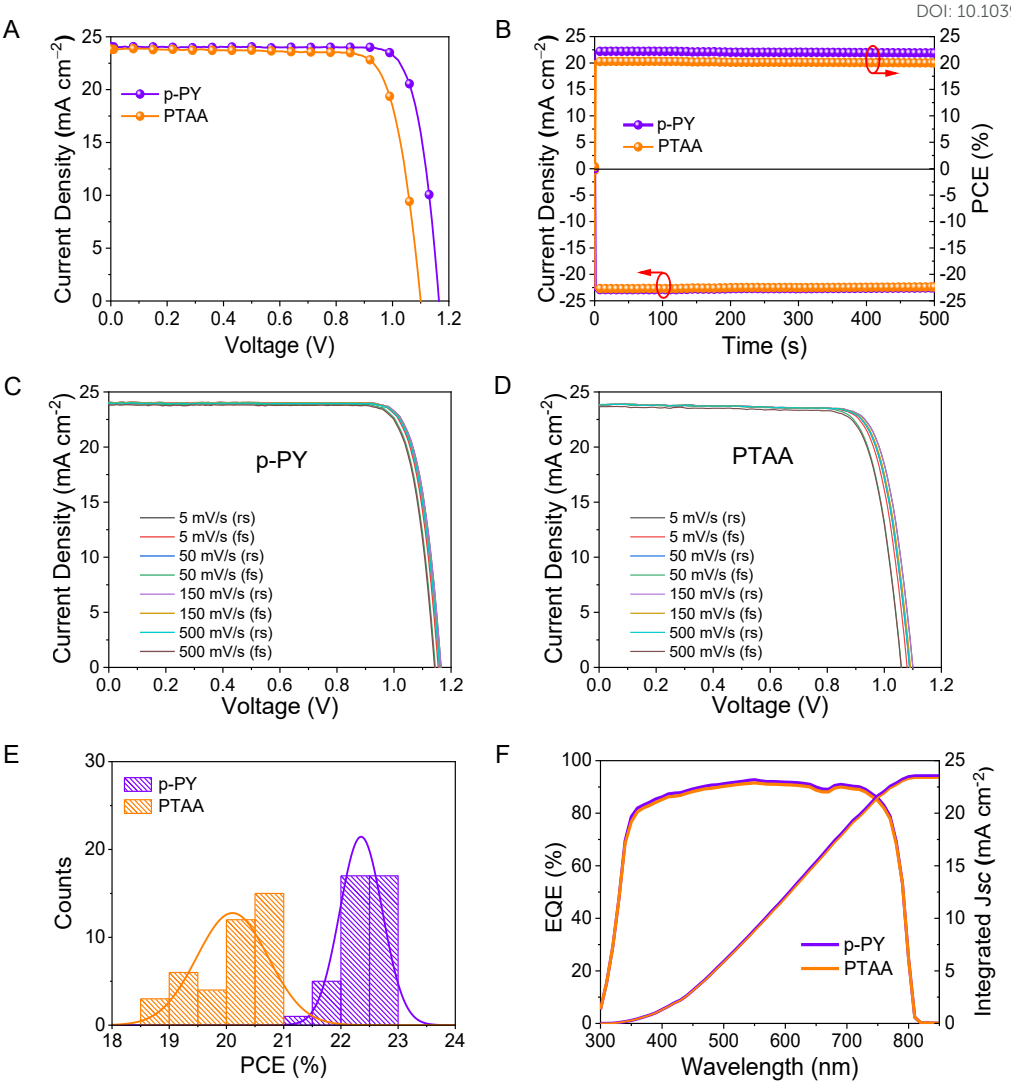

Figure 3. Photovoltaic performances. (**A**) *J-V* curves of the champion PSCs based on dopant-free p-PY and PTAA; (**B**) Stabilized power output at the maximum power point (MPP) under simulated AM 1.5 G solar illumination at 100 mW cm^{-2}; *J-V* curves of the (C) p-PY and (D) PTAA based devices with different voltage sweep (**E**) Statistical performance of the PSCs based on p-PY and PTAA. (**F**) EQE spectra with the integrated J_{SC} for the champion PSCs based on p-PY and PTAA.

View Article Online
DOI: 10.1039/D2EE00433J

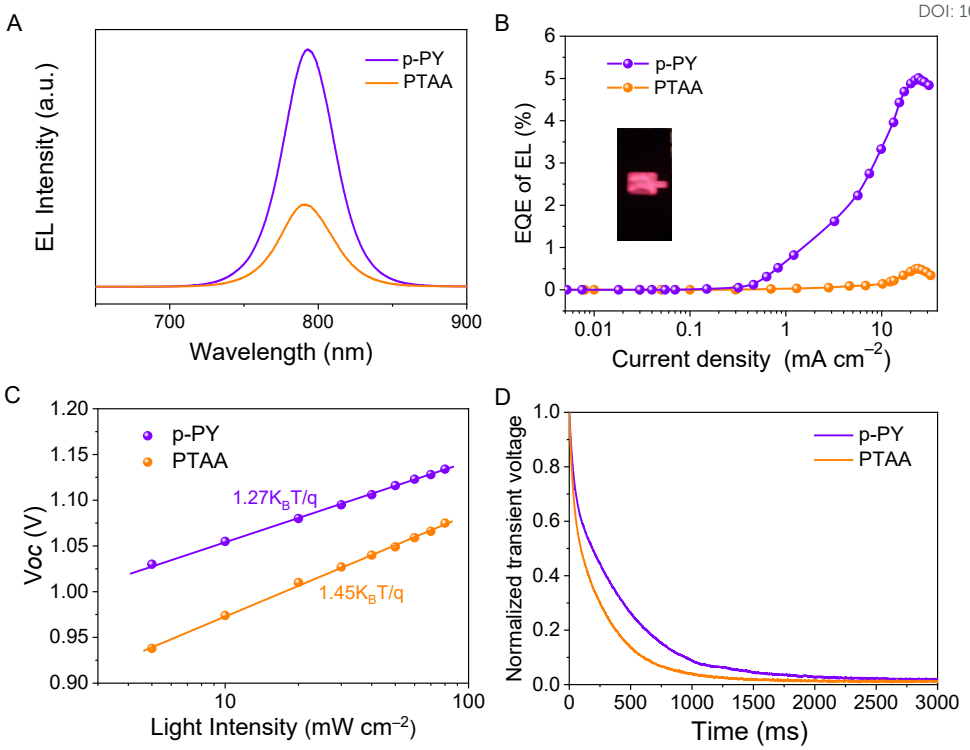

Figure 4. Carrier dynamic characterization of the p-PY and PTAA-based PSCs. (**A**) The EL spectrum of the p-PY and PTAA-based PSCs; (**B**) EQE of EL of the p-PY and PTAA-based devices while operating as LEDs; (**C**) V_{OC} versus illumination intensity for the p-PY and PTAA-based devices; (**D**) Normalized transient photovoltage decay for the p-PY and PTAA-based devices.

View Article Online
DOI: 10.1039/D2EE00433J

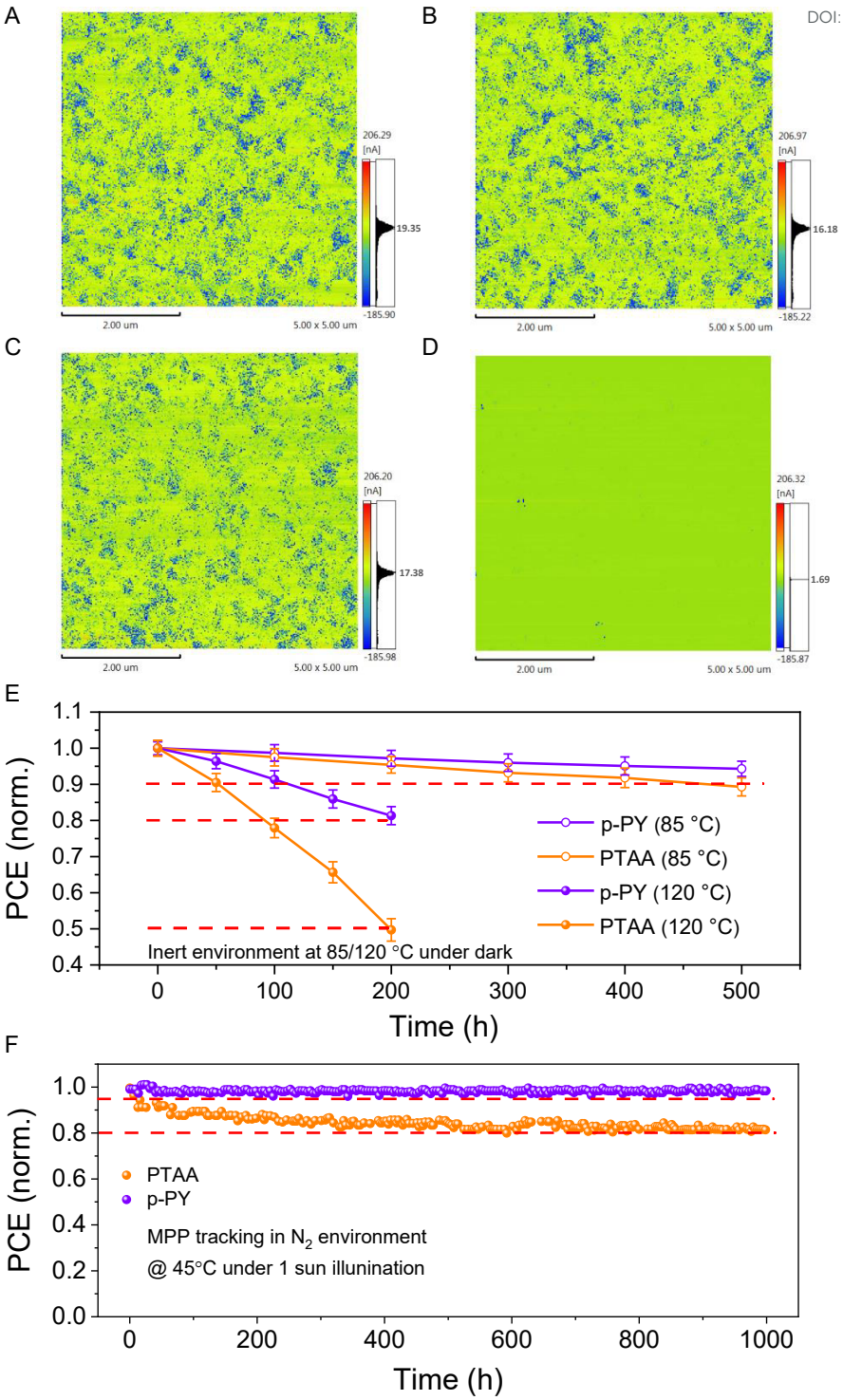

Figure 5. Thermal and light stability of the p-PY and PTAA-based PSCs. c-AFM images of (**A, C**) p-PY and (**B, D**) PTAA films on ITO glass substrates before and after aging at 120 ˚C for 200 h; (**E**) Thermal stability of the

View Article Online
DOI: 10.1039/D2EE00433J

unencapsulated devices stressed at 120 °C in N_2 atmosphere in the dark. Six identically prepared devices were aged at each condition respectively; (**F**) Light soaking stability of unencapsulated devices under 1 sun equivalent white-light LED array illumination with continuous MPP tracking at 45 °C in N_2 atmosphere.